Proceedings of GT2008
ASME Turbo Expo 2008: Power for Land, Sea and Air
May 14-17, 2008, Berlin, Germany

GT2008-50737

Calibration of CFD Model for Mist/Steam Impinging Jets Cooling

Ting Wang and T. S. Dhanasekaran
Energy Conversion and Conservation Center
University of New Orleans
New Orleans, LA 70148-2220, USA

ABSTRACT

In the heavy-frame advanced turbine systems, steam is used as a coolant for turbine blade cooling. The concept of injecting mist into the impinging jets of steam was experimentally proved as an effective way of significantly enhancing the cooling effectiveness in the laboratory under low pressure and temperature conditions. However, whether mist/steam cooling is applicable under actual gas turbine operating conditions is still subject to further verification. Recognizing the difficulties of conducting experiments in an actual high-pressure, high-temperature working gas turbine, a simulation using a CFD model calibrated with laboratory data would be an opted approach. To this end, the present study conducts a CFD model calibration against the database of two experimental cases including a slot impinging jet and three rows of staggered impinging jets.

Using the experimental results, the CFD model has been tuned by employing different turbulence models, computational cells, wall y^+ values, and selection of near-wall functions. In addition, the effect of different forces (e.g. drag, thermophoretic, Brownian, and Saffman's lift force) are also studied. None of the models are good predictors for all the flow regions from near the stagnation region to far-field downstream of the jets. Overall speaking, both the standard k-ε and RSM turbulence models perform better than other models. The RSM model has produced the closest results to the experimental data due to its capability of modeling the non-isotropic turbulence shear stresses in the 3-D impinging jet fields. For the 3-D flow fields, the nearest element from the wall must be set to approximately unity ($y^+ \approx 1$) to capture the correct flow structure. The simulated results showed that the calibrated CFD model could predict the heat transfer coefficient of steam-only case within 2 to 5% deviations from the experimental results for all the cases. When mist is employed, the prediction of wall temperatures is within 5% for a slot jet and within 10% for three-row jets.

Keywords: Impinging jets, mist cooling, heat transfer enhancement, two-phase flow, gas turbine blade cooling

NOMENCLATURE

b	slot width (m)
C	concentration (kg/m^3)
d	diameter of round jet (m)
h	convective heat transfer coefficient (W/m^2-K)
H	target distance (channel height, m)
k	turbulent kinetic energy (m^2/s^2)
k_c	mass transfer coefficient
K	thermophoretic coefficient
m	mass (kg)
q''	wall heat flux (W/m^2)
Re	Reynolds number
T_w	wall temperature (^oC)
T_j	jet temperature (^oC)
TC	Stochastic tracking time constant
v	velocity (m/s)

Greek

ε	turbulence dissipation (m^2/s^3)
λ	thermal conductivity (W/m-K)

Subscript

j	jet
p or d	particle or droplet

INTRODUCTION

Jet impingement heat transfer has been employed for many industrial applications like the cooling of turbine blades and electrical equipment, drying of paper and textiles, and annealing of metals. In the gas turbine industry, there is a continuous need for increasing the inlet temperature to achieve higher thermal efficiency, which

eventually demands significant cooling enhancement on the turbine blades. The extensive experimental studies under laboratory conditions have proven that the concept of injecting mist (tiny water droplets) into the single-phase coolant flow is an effective approach to enhance cooling in a straight pipe [1 & 2], in a 90-degree bend [3], in a slot impinging jet on both a flat and a concave surfaces [4 & 5], and in multiple impinging jets [6 & 7]. Typically, an average cooling enhancement of 50 - 100% was achieved by injecting 1-3% (wt.) mist into the steam flow. Very high local cooling enhancement of 200 - 300% was observed in the tube and on a flat surface, and cooling enhancement above 500% was observed when steam flow passed the 90-degree bend.

The concept of using mist/steam to enhance cooling effectiveness is based on the following features: (a) latent heat of evaporation, (b) increased specific heat, (c) steeper temperature gradient near the wall, (d) lower bulk temperature, (e) increased flow mixing induced by steam-droplet interactions and droplet dynamics, and (f) additional momentum and mass transfer induced by the thrust of evaporation of liquid droplets on/near the wall. A model for mist/steam jet cooling was developed by Li et al. [8]. This model considered the total heat flow to be comprised of three components: single-phase-like heat flow, boundary layer quenching effect accounting for heat flow leaving the surface through the steam, and added heat flow occurring in brief contacts with impacting droplets. Their analysis showed that the heat conduction from the wall to droplet was the dominant enhancement mechanism. The quenching effect of droplets in the steam flow became important when the mist concentration was high. The heat transfer to small droplets was mainly through the steam while larger droplets hit and cooled the heated wall by direct heat conduction. An extensive review of relevant mist cooling literatures has been conducted by Guo and Wang [1] and is not repeated here.

Numerous experimental and numerical investigations on the single-phase impinging confined jets have been conducted and are available in the literature. Chou and Hung [9] conducted an analytical study for cooling of an isothermal heated surface with a confined slot jet. They also performed a numerical study for the fluid flow and heat transfer of slot jet impingement with an extended nozzle [10]. Laschefski et al. [11] numerically analyzed the velocity field and heat transfer in rows of rectangular impinging jets in the transient state. Cziesla et al. [12] simulated turbulent flow issued from a slot jet array using a subgrid stress model. In 1998, Yang and Shyu [13] presented numerical predictions on the fluid flow and heat transfer characteristics of multiple impinging slot jets with an inclined confinement surface. Tzeng et al. [14] employed eight turbulence models including one standard and seven low-Reynolds number k-ε models to predict the heat transfer performance of multiple impinging jets. Validation results indicated that the prediction by each turbulence model depended on grid distributions and numerical scheme used in spatial discretization. Recently, Goodro et al. [15] studied the effect of hole spacing on jet array impingement heat transfer on flat plate and showed that spatially-averaged Nusselt numbers for 8D hole spacing are generally higher than values for 12D hole spacing.

As far as the studies on two-phase impinging jet are concerned, Shimizu et al. [16] experimentally investigated the heat transfer of an axisymmetric jet impinging on a flat surface. They used a suspension consisting of nitrogen gas and graphite particles of 10μm diameter and varied the initial loading ratio up to 2.5. They have shown that the stagnation point heat transfer coefficient obtained at the highest loading ratio was found to be six times as large as the single-phase flow. Yoshida et al. [17] conducted experiments on two-dimensional impinging jet with gas-solid suspensions. These experiments provided detailed data on the turbulence structure, and on the basis of the information, clarified the heat transfer mechanism of the gas-solid impinging jet. These studies did not include phase change, and that will be modeled by the present study.

Impinging liquid spray cooling involves liquid evaporation and bears some similarity of mist impinging cooling, but the liquid droplets in the spraying cooling are typically vary large (50μm - 2 mm) and are transported dominantly by droplets inertia with minimal entrained gas flow. Therefore, the two-phase flow physics and flow field of liquid spray cooling are different from mist impinging jet cooling.

Even though there was not much information on the numerical studies of the impinging jet with mist in a steam flow, similar studies applied to mist in the air film cooling were seen in the literature. Li and Wang [18-19] simulated mist/air film cooling and showed that a small amount of mist injection (2% of the coolant mass flow rate) could increase the adiabatic cooling effectiveness about 30% ~ 50% under low temperature, velocity and pressure conditions similar to those in the laboratory. The effect of different flow parameters, injection hole configuration, and coolant supply plenum on the cooling effectiveness were also studied. Considering the effect of blade internal cooling on the film cooling over the blade outer surface, Li and Wang [20] further presented the mist/air film cooling heat transfer coefficient under non-adiabatic wall condition including conjugate condition employing internal channel cooling beneath the blade surface. The results of conjugate 2D cases indicated that heat conduction from downstream to upsteam along the solid wall are strong. The streamwise heat even conducted back from a distance of 5-slot widths downstream to the neighborhood of the jet hole. Terekhov and Pakhomov [21] conducted a numerical study of the near-wall droplet jet in a heated tube. They examined the effects of droplet diameter, the blowing ratio, and the wall heat flux on cooling enhancement. Recently, Li and Wang [22] computationally investigated the mist cooling performance on the leading edge and curved surfaces of a stationary turbine blade and found that the maximum mist cooling

enhancement was approximately 60% on the pressure side and 30% on the suction side.

It should be noted that mist/air flow and mist/steam flow are thermodynamically different. Mist/air is a two-component, two-phase flow where the evaporation process of the water droplets is controlled by the partial pressure of the water vapor in the air and not by the total pressure of the mixture. Mist/steam is a one-component, two-phase flow in which the evaporation process of the water droplets is controlled by the steam pressure. Generally under the same pressure and the same temperature, the droplets within mist/air flow are more likely to evaporate than those within mist/steam flow. When the surrounding temperature is above the boiling temperature, the vaporization process for both mist/steam and mist/air is identical; both are subjected to the total pressure of the mixture.

In the open literature, no documents have indicated that this concept of mist/steam cooling has ever been tested under an actual gas turbine (high temperature and high pressure) working condition. Recognizing the difficulty and cost in conducting an experiment at high Reynolds number and under elevated pressure and temperature conditions, implementing CFD simulation will be an opted approach to providing preliminary flow and heat transfer physics to guide decision-making on conducting experiments.

The present investigation focuses on calibrating the CFD model with experimental data taken under low temperature and pressure conditions. The calibrated CFD model will be used to predict the potential mist/steam heat transfer enhancement under actual gas turbine operating conditions in the future. The calibration is carried out with the available database of experimental results of a slot jet [4] and multiple rows of staggered jets [7].

NUMERICAL MODEL

Test Section

Figure 1 shows the schematic diagram of the confined multiple-row impinging jet experimental test section employed by Wang et al. [7]. The same test section was used for a slot impinging jet by replacing the upper plate. As shown in the figure, the multiple steam jets with mist are impinging on the target wall and split at the stagnation line in either sides of x-direction and proceeds to a settling plenum before exit through circular tubes. The settling plenum was used to minimize disturbance that could be caused by directly exhausting the spent steam to the tubes. From a computational point of view, two different domains are considered: the basic domain (solid line in Fig.1) which includes only the confined region of 0.125m long and the extended domain (dotted line in Fig. 1) which includes the settling plenum and a short length of tube. Additional details on the experimental test set-up can be obtained from references [4-7]. The geometry details of the two experimental models are shown in Fig. 2. The slot width is 7.5 mm, the jet hole diameter is 8.1mm, the target wall distance is 22.5 mm (2.8d), and the confined passage length is 250 mm. For multiple jets, the jet centers are spaced at 25 mm (3d) apart. The dimensions of the target distance and domain length are kept constant for all cases. The target wall is heated uniformly by joule heating. Due to flow symmetry, only half-a-portion of the slot jet domain is calculated. For the multiple-row jets, one-quarter of the actual flow domain is computationally modelled.

It should be noted that the mist was not generated by an atomizer near the jet issuing slot or holes; rather, the mist was generated and mixed with saturated steam in a mixer approximate 3 feet away from the test section and was then transported to the settling chamber. This process provides a true mist flow with liquid droplets suspending in the main flow, which is different from the sprayed flow. A spray flow will involve active liquid droplet break-up, coalescence, and precipitation. It should be noted that no rotating effect is included in this study, so the results of this study can not be directly applied to gas turbine application without further verification of the rotating effect.

Numerical Method

A feasible method to simulate the steam flow with mist injection is to consider the droplets as a discrete phase since the volume fraction of the liquid is usually small (e.g. 5% mist by weight gives approximately 0.08% in volume.) The trajectories of the dispersed phase (droplets) are calculated by the Lagrangian method by tracking each droplet from its origin. The impact of the droplets on the continuous phase is considered as source terms to the governing equations of mass, momentum and energy. Two components (water and water vapor) are simulated in the impinging jet flow. Various turbulence models are used with standard and enhanced near-wall treatment to the continuous phase (stream).

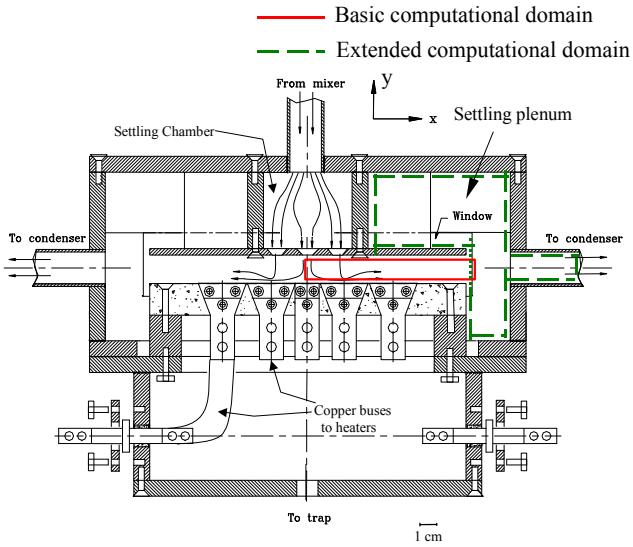

Figure 1 Experimental setup (Wang et. al. [7]) denoting the two computational domains considered.

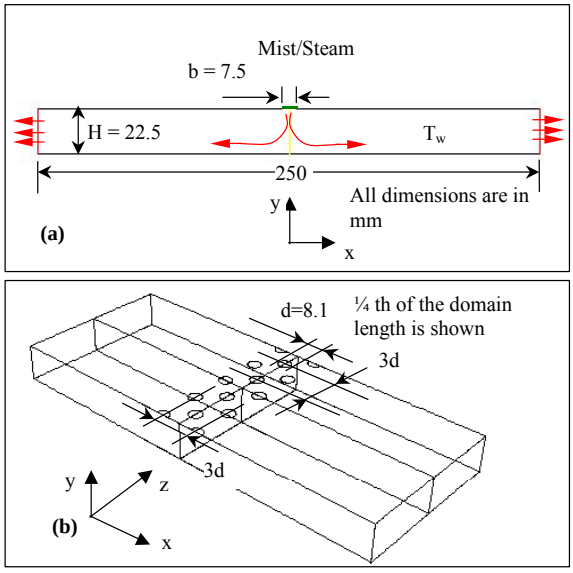

Figure 2 Geometry details for basic computational domain: (a) slot jet (b) three-row staggered jets. Only 1/4th of the domain length is shown.

Governing Equations

The 3-D time-averaged steady-state Navier-Stokes equations as well as equations for mass and energy are solved. The governing equations for conservation of mass, momentum, and energy are given as:

$$\frac{\partial}{\partial x_i}(\rho u_i) = S_m \tag{1}$$

$$\frac{\partial}{\partial x_i}(\rho u_i u_j) = \rho \bar{g}_j - \frac{\partial P}{\partial x_j} + \frac{\partial}{\partial x_i}\left(\tau_{ij} - \rho\overline{u'_i u'_j}\right) + F_j \tag{2}$$

$$\frac{\partial}{\partial x_i}(\rho c_p u_i T) = \frac{\partial}{\partial x_i}\left(\lambda \frac{\partial T}{\partial x_i} - \rho c_p \overline{u'_i T'}\right) + \mu\Phi + S_h \tag{3}$$

where τ_{ij} is the symmetric stress tensor defined as

$$\tau_{ij} = \mu\left(\frac{\partial u_j}{\partial x_i} + \frac{\partial u_i}{\partial x_j} - \frac{2}{3}\delta_{ij}\frac{\partial u_k}{\partial x_k}\right) \tag{4}$$

The source terms (S_m, F_j and S_h) are used to include the contribution from the dispersed phase. $\mu\Phi$ is the viscous dissipation.

In mist/air cooling, water droplets evaporate, and the vapor diffuses and is transported into its surrounding flow. Different from the mist/air flow, no species transport equation is used in the mist/steam flow since steam is the only main flow medium.

The terms of $\rho\overline{u'_i u'_j}$ and $\rho c_p \overline{u'_i T'}$, represent the Reynolds stresses and turbulent heat fluxes. The Reynolds number of the main flow (based on the duct height and the inlet condition) is about 22,500 in this study.

Turbulence Models

Standard k-ε Model – The standard k-ε model, which, based on the Boussinesq hypothesis, relates the Reynolds stresses to the mean velocity as

$$-\rho\overline{u'_i u'_j} = \mu_t\left(\frac{\partial u_i}{\partial x_j} + \frac{\partial u_j}{\partial x_i}\right) - \frac{2}{3}\rho k\delta_{ij} \tag{5}$$

The turbulent viscosity, μ_t is given by

$$\mu_t = \rho C_\mu k^2/\varepsilon \tag{6}$$

where C_μ is a constant. The equations for the turbulent kinetic energy (k) and the dissipation rate (ε) are:

$$\frac{\partial}{\partial x_i}(\rho u_i k) = \frac{\partial}{\partial x_i}\left[\left(\mu + \frac{\mu_t}{\sigma_k}\right)\frac{\partial k}{\partial x_i}\right] + G_k - \rho\varepsilon . \tag{7}$$

$$\frac{\partial}{\partial x_i}(\rho u_i \varepsilon) = \frac{\partial}{\partial x_i}\left[\left(\mu + \frac{\mu_t}{\sigma_\varepsilon}\right)\frac{\partial \varepsilon}{\partial x_i}\right] + C_{1\varepsilon}G_k\frac{\varepsilon}{k} - C_{2\varepsilon}\rho\frac{\varepsilon^2}{k} . \tag{8}$$

The term G_k is the generation of turbulent kinetic energy due to the mean velocity gradients.

The turbulent heat flux can be modeled with the turbulent heat conductivity (λ_t).

$$\rho c_p \overline{u'_i T'} = -\lambda_t\frac{\partial T}{\partial x_i} = -c_p\frac{\mu_t}{Pr_t}\frac{\partial T}{\partial x_i} \tag{9}$$

The constants $C_{1\varepsilon}$, $C_{2\varepsilon}$, C_μ, σ_k, and σ_ε used are: $C_{1\varepsilon}$ = 1.44, $C_{2\varepsilon}$ = 1.92, C_μ = 0.09, σ_k = 1.0, σ_ε =1.3 [23]. The turbulent Prandtl number, Pr_t, is set to 0.85,.

Enhanced Wall Function – The above k-ε model is mainly valid for a high Reynolds number fully turbulent flow. Special treatment is needed in the region close to the wall. The enhanced wall function is one of several methods that model the near-wall flow. In the enhanced wall treatment, a two-layer model is combined with the wall functions. The whole domain is separated into a viscosity-affected region and a fully turbulent region by defining a turbulent Reynolds number, Re_y,

$$Re_y = yk^{1/2}/\nu \tag{10}$$

where y is the distance from the wall. The standard k-ε model is used in the fully turbulent region where Re_y > 200, and the one-equation model of Wolfstein [24] is used in the viscosity-affected region with Re_y < 200. The turbulent viscosities calculated from these two regions are blended with a blending function (θ) to smoothen the transition.

$$\mu_{t,enhanced} = \theta\mu_t + (1-\theta)\mu_{t,l} \tag{11}$$

where μ_t is the viscosity from the k-ε model of high Reynolds number, and $\mu_{t,l}$ is the viscosity from the near-wall one-equation model. The blending function is equal

to 0 at the wall and 1 in the fully turbulent region. The linear (laminar) and logarithmic (turbulent) laws of the wall are also blended to make the wall functions applicable throughout the entire near-wall region.

Reynolds Stress Model – The turbulence in the impinging flow could be anisotropic and nonequilibrium with multiscaled integral and dissipation length scales. Therefore, a Reynolds stress model (RSM), a second-moment closure, is considered in this study. The Reynolds stress transport equation is given as

$$\frac{\partial}{\partial x_k}\left(\rho u_k \overline{u'_i u'_j}\right) = -\frac{\partial}{\partial x_k}\left[\rho u_k \overline{u'_i u'_j u'_k} + \overline{P(\delta_{kj}u'_i + \delta_{ik}u'_j)} + \mu\frac{\partial}{\partial x_k}\left(\overline{u'_i u'_j}\right)\right] - \rho\left(\overline{u'_i u'_k}\frac{\partial u_j}{\partial x_k} + \overline{u'_j u'_k}\frac{\partial u_i}{\partial x_k}\right) + \overline{P\left(\frac{\partial u'_i}{\partial x_j} + \frac{\partial u'_j}{\partial x_i}\right)} - 2\mu\overline{\frac{\partial u'_i}{\partial x_k}\frac{\partial u'_j}{\partial x_k}} \quad (12)$$

The diffusive term on the right-hand side can be modeled as

$$-\frac{\partial}{\partial x_k}\left[\rho u_k \overline{u'_i u'_j u'_k} + \overline{P(\delta_{kj}u'_i + \delta_{ik}u'_j)} + \mu\frac{\partial}{\partial x_k}\left(\overline{u'_i u'_j}\right)\right] = \frac{\partial}{\partial x_k}\left(\frac{\mu_t}{\sigma_k}\frac{\partial}{\partial x_k}\left(\overline{u'_i u'_j}\right)\right) \quad (13)$$

The second term on the right-hand side of Eq. (12) is the production term, and it is notated as G_{ij}.

$$G_{ij} = -\rho\left(\overline{u'_i u'_k}\frac{\partial u_j}{\partial x_k} + \overline{u'_j u'_k}\frac{\partial u_i}{\partial x_k}\right) \quad (14)$$

The third term is the pressure-strain term, which can be modeled as:

$$\overline{P\left(\frac{\partial u'_i}{\partial x_j} + \frac{\partial u'_j}{\partial x_i}\right)} = C_1\rho\frac{\varepsilon}{k}\left(\overline{u'_i u'_j} - \frac{2}{3}\delta_{ij}k\right) - C_2\left[A_{ij} - \frac{1}{3}\delta_{ij}A_{kk}\right] \quad (15)$$

where $A_{ij} = G_{ij} - \frac{\partial}{\partial x_k}\left(\rho u_k \overline{u'_i u'_j}\right)$. The constants C_1 and C_2 are 1.8 and 0.6, respectively. By assuming the dissipation is isotropic, the last term in Eq. (12) can be approximated by:

$$2\mu\overline{\frac{\partial u'_i}{\partial x_k}\frac{\partial u'_j}{\partial x_k}} = \frac{2}{3}\delta_{ij}\rho\varepsilon \quad (16)$$

Modeling of the turbulent heat flux is similar as in the k-ε model. The turbulent kinetic energy and its dissipation rate can be calculated from the Reynolds stresses.

Other Models – Ignoring details here, the turbulence models adopted in this study also include RNG k-ε model, k-ω model, and the shear-stress transport (SST) k-ω model. The RNG k-ε model was derived using renormalization group theory [25]. It has an additional term in the ε-equation to improve the accuracy for rapidly strained flows. The effective viscosity is used to account for low-Reynolds-number effect. Theoretically, this model is more accurate and reliable than the standard k-ε model. The standard k-ω model is an empirical model based on transport equations for the turbulent kinetic energy (k) and the specific dissipation rate (ω), which can also be considered as the ratio of ε to k [26]. The low-Reynolds-number effect is accounted for in the k-ω model. The SST model is a mixture of the k-ω model and the k-ε model: close to the wall it becomes the k-ω model while in the far field the k-ε model is applied [27].

Discrete-Phase Model (Water Droplets)

Droplet Flow and Heat Transfer – Based on Newton's 2nd Law, the droplet motion in airflow can be formulated by

$$m_p d\mathbf{v_p}/dt = \sum \mathbf{F} \quad (17)$$

where $\mathbf{v_p}$ is the droplet velocity (vector). The right-hand side is the combined force acting on the droplet, which normally includes the hydrodynamic drag, gravity, and other forces such as Saffman's lift force [28], thermophoretic force [29], and Brownian force [30], etc.

Without considering the radiation heat transfer, droplet's heat transfer depends on convection and evaporation as given in the following equation.

$$m_p c_p \frac{dT}{dt} = \pi d^2 h(T_\infty - T) + \frac{dm_p}{dt}h_{fg} \quad (18)$$

where h_{fg} is the latent heat. The convective heat transfer coefficient (h) can be obtained with an empirical correlation [31 and 32]:

$$Nu_d = \frac{hd}{\lambda} = 2.0 + 0.6\,Re_d^{0.5}\,Pr^{0.33} \quad (19)$$

where Nu_d is the Nusselt number, and Pr is the Prandtl number.

Theoretically, evaporation can occur at two stages: (a) when the temperature is higher than the saturation temperature (based on local water vapor concentration), water evaporates, and the evaporation is controlled by the water vapor partial pressure until 100% relative humidity is achieved; (b) when the boiling temperature (determined by the air-water mixture pressure) is reached, water continues to evaporate. In this study, the main flow medium is steam, so the evaporation of the water droplets is not controlled by the partial water vapor (as in the mist/air flow), rather it is controlled by the total pressure of the steam flow, i.e. by the boiling temperature as in [33]:

$$-\frac{dm_p}{dt} = \pi d^2\left(\frac{\lambda}{d}\right)(2.0 + 0.46Re_d^{0.5})\ln\left(1 + c_p(T_\infty - T)/h_{fg}\right)/c_p \quad (20)$$

where c_p is the specific heat of the bulk flow.

Stochastic Particle Tracking – The turbulence models discussed above can only obtain time-averaged velocity. Using this velocity to trace the droplet will result in an averaged trajectory identical to the streamline. In a real flow, the instantaneous velocity fluctuation would make the droplet move around this averaged track. However,

the instantaneous velocity is not simulated in the current computation because the turbulence is modeled in time-averaged terms. One way to simulate the instantaneous turbulent effect on droplet dispersion is to "improvise" the random turbulent fluctuation by using the stochastic tracking scheme [34]. Basically, the droplet trajectories are calculated by imposing the instantaneous flow velocity ($\bar{u} + u'$) rather than the average velocity ($\bar{u}$). The velocity fluctuation is then given as:

$$u' = \zeta\left(\overline{u'^2}\right)^{0.5} = \zeta(2k/3)^{0.5} \qquad (21)$$

where ζ is a normally distributed random number. This velocity will apply during the characteristic lifetime of the eddy (t_e), which is a time scale calculated from the turbulent kinetic energy and dissipation rate. After this time period, instantaneous velocity will be updated with a new ζ value until a full trajectory is obtained. Note, when the RSM model is used, the velocity fluctuation is independently decided in each direction. When the stochastic tracking is applied, the basic interaction between droplets and continuous phase stays the same, which is accounted by the source terms in the conservation equations. The source terms are not directly but rather indirectly affected by the stochastic method; so formulation of the source terms is not affected by implementing the stochastic tracking method. For example, the drag force between a water droplet and the steam flow depends on the slip velocity calculated by the averaged Navier-Stokes equations, and the droplet velocity calculated by the Lagrangian equation (17). When the stochastic tracking method is used, a random velocity fluctuation is imposed at an instant of time, and the drag force will be calculated based on this instantaneous slip velocity. The source term associated with this instantaneous drag force enters into the momentum equation without any additional formulation. For a steady-state calculation, the "instant of time" means "each iteration step."

Boundary Conditions

Continuous flow (Steam) – Various boundary conditions are assigned to the two different impinging cases. In common, steam is considered as continuous flow and mist is considered as discrete flow for all the models. In the slot jet model, the uniform inlet velocity of 27 m/sec (Reynolds number of 22,500 based on jet width b) is assigned in negative y-direction. Since no experimental measurement of the issuing jet velocity profile is available, in view of the thin plate the jet holes were drilled through, the velocity profile should be close to a uniform profile with a very thin boundary layer effect. The saturated temperature of steam at the inlet was 105°C. At the target wall, the constant heat flux of 20,900 W/m^2 is applied. Symmetric boundary condition has been used at the centreline parallel to the impinging direction (Fig. 2a). The symmetric condition imposes zero normal velocity at the symmetry plane and zero normal gradients of all variables at the symmetry plane. In the case of multiple-row jets model, constant inlet velocity of 32.75 m/sec (Reynolds number of 15,000 based on jet diameter, d) with saturated steam inlet temperature of 103°C is assigned. Due to symmetry, one-quarter of the test domain is considered as the computational domain. A constant heat flux of 13,400 W/m^2 is applied on the target wall. Two symmetric planes are assumed; one at the x-y plane and another one at the y-z plane as shown in Fig. 2b. All the side and top walls in the computational domain are assigned as adiabatic walls with non-slip velocity boundary condition. The inlet turbulence intensity is specified as 1%. The flow exit of computational domain is assumed to be at a constant pressure of 1 atm.

Discrete flow (mist) – The fine water droplet with a uniform arithmetic mean diameter of 10 μm are injected. In the slot jet cases, the particles are injected from equally spaced 10 locations at the inlet. Two mass concentration ratios (mist/steam) of 1% and 2% are simulated. In the 3-D multiple-row jets case, mist ratio of 1.5% (0.0000177 kg/s water droplets) is simulated.

Computational Cells

The computational domain has been discretized to fine cells to conduct the simulation. Fig. 3a shows the computational grid of the 2-D slot jet, which contains structured quad elements. The total number of 9,000 cells is used in this model. Fig. 3b shows the computational mesh of the three-row jet case. The domain is completely constructed by hexahedral elements. To accurately predict possible recirculation, separation, and reattachment zones, the cells have been clustered towards the wall to obtain appropriate y+ value less than 1. A total of 480,000 cells are used for the 3-D three-row jet case.

The computation has been carried out using the commercial CFD software FLUENT (Version 6.2.16) from Ansys, Inc. The simulation uses the segregated solver, which employs an implicit pressure-correction scheme and decouples the momentum and energy equations. The SIMPLE algorithm is used to couple the pressure and velocity. Second order upwind scheme is selected for spatial discretization of the convective terms. The second order accuracy is obtained by calculating quantities at cell faces using multidimensional linier reconstruction approach [34]. The computation is conducted for the steam field (continuous phase) first. After obtaining an approximate converged flow field of the steam, the dispersed phase of droplet trajectories are calculated. At the same time, drag, heat and mass transfer between the droplets and the steam flow are calculated. Variable property values are calculated using polynomial equations for steam and piecewise approximation for water droplets. It was discovered that the property database for water vapor and steam in Fluent is not sufficient and gives unreasonable results such as predicting temperature lower than Wet Bulb temperature after water droplet

evaporation. A detailed database has been incorporated through Function statement.

Iterations proceed alternatively between the continuous and discrete phases. Ten iterations in the continuous phase are conducted between two iterations of the discrete phase. Converged results are obtained after the residuals satisfy mass residual of 10^{-4}, energy residual of 10^{-6}, and momentum and turbulence kinetic energy residuals of 10^{-5}. These residuals are the summation of the imbalance in each cell, scaled by a representative for the flow rate. The computation was carried out in parallel processing on two dual-core Pentium clusters with 10 nodes and 6 nodes, respectively.

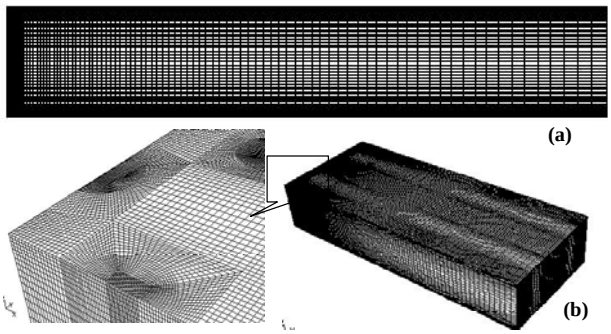

Figure 3 Computational domain:(a) Slot jet and (b) multiple-row of staggered jets.

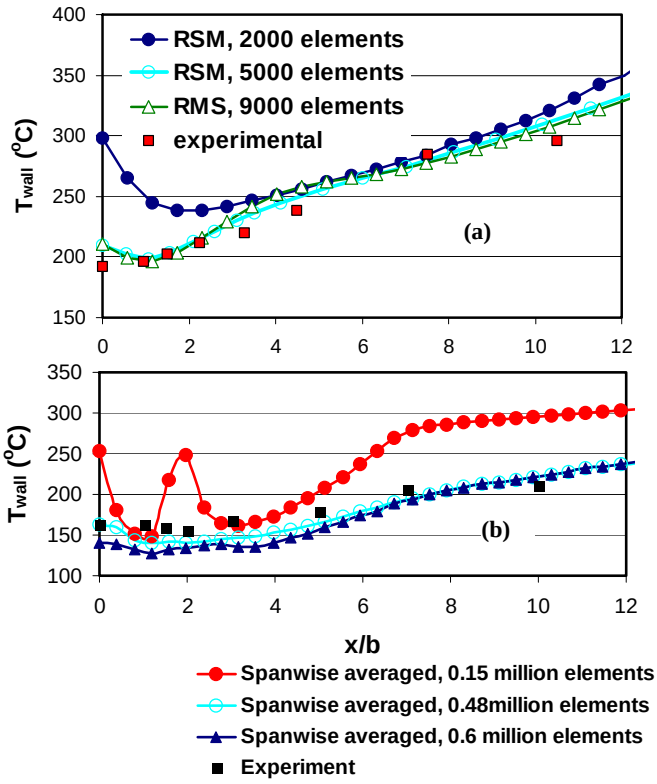

Figure 4 Grid sensitivity study: (a) slot jet and (b) three-row jets.

Grid sensitivity study – A grid sensitivity test has been carried out on both the slot jet and the three-row jets cases, as shown in Fig. 4. In the slot jet calculation, it is verified that the result of wall temperature distribution is negligibly affected by number of cells above 5,000. In the three-row jets case, there is a big change from 0.15 million cells to 0.48 million cells, but the variation is limited between 0.48 million and 0.6 million cells cases. Although grid-independence has not been achieved, the results show a negligible difference in the far-field at x/b >7 and approximately 10% difference in the stagnation region. Therefore in the 3-D cases, grid independent results are not claimed in this study, rather it is claimed that the further refinement of the cells will generate results within less than 10% difference.

RESULTS AND DISCUSSION

Results of Slot Impinging Jet

Effect of turbulence models – In the process of calibrating the CFD model, initially, computation was carried out with various turbulence models including Standard k-ε, RNG, Reynolds Stress Model (RSM), K-ω, and SST on the slot jet for steam only case. The computed temperatures on the target wall by all the turbulence models are shown spreading within a ±15% band across the experimental data in Fig. 5a. The RSM model provides the best overall prediction with an average of 5% deviation from the experimental data. The standard k-ε model provides the second best prediction. This model predicts better than RSM near the stagnation point and in the region between 3b and 5b, but in the far field it does not do well. The predictions from other models like RNG, K-ω, and SST are less promising and show larger deviations from the experimental data.

The effect of the turbulence model has been verified for the steam/mist case also as shown in Fig. 5b. Three turbulence models including Standard k-ε, RNG, RSM are considered for this study, as those models performed better than other models in the steam only case. The results show that all the three turbulence models predict the same value near stagnation region up to x/b = 3.0 and beyond that k-ε and RSM models predicts closer to experimental values as seen in the steam only case.

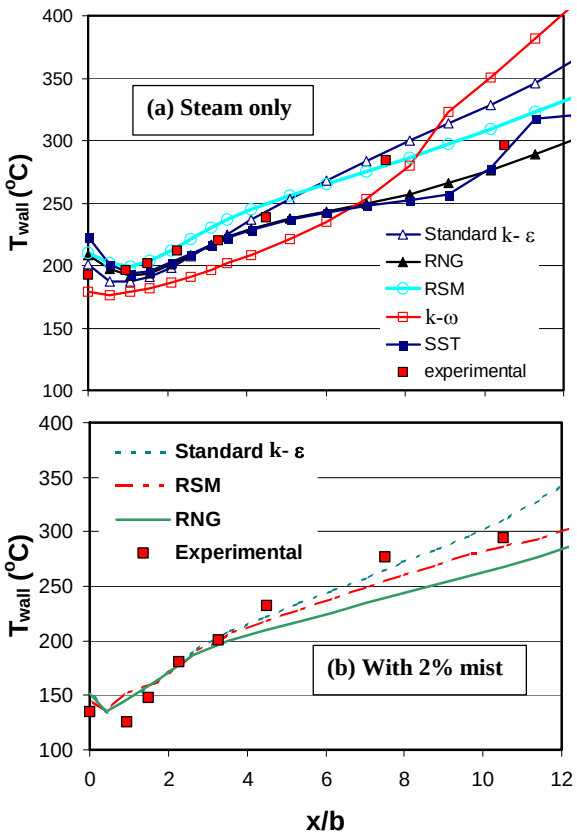

Figure 5 Wall temperature distribution of slot jet model.

To investigate the reason for the wide range of deviation in the predicted results of the steam only case, velocity vectors are plotted for various turbulence models as shown in the Fig. 6. The figure clearly shows the large difference in the flow field predicted by various turbulence models, especially the center location of the recirculation zone (CRZ). The CRZ is located midway between confined walls at x/b = 3 in the flow field calculated by the standard k-ε and k-ω models (Figs. 6a and d). The remaining models predict the center location of CRZ at about x/b = 6. It is interesting to observe that the closer the center of CRZ to the stagnation line the stronger the forced convection cooling and the lower the wall temperature near the stagnation point. In the meantime, the closer the center of the CRZ is to the stagnation line, the smaller the recirculation area is induced. This results in a quicker spread of impinging jet and less cooling fluid traveling near the target wall, and downstream (e.g. Fig. 6d vs. 6e). Hence, warmer wall temperature is in the far field (x/b >9). The order of closeness to the center of CRZ and the stagnation line is k-ω, k-ε, RNG, RSM, and SST, which leads to the predicted stagnation temperature following in the ascending order and the predicted far-field wall temperature in the descending order. Figure 5 shows that k-ω, k-ε, and RNG turbulence models over predict the far-field (x/b>9) wall temperature.

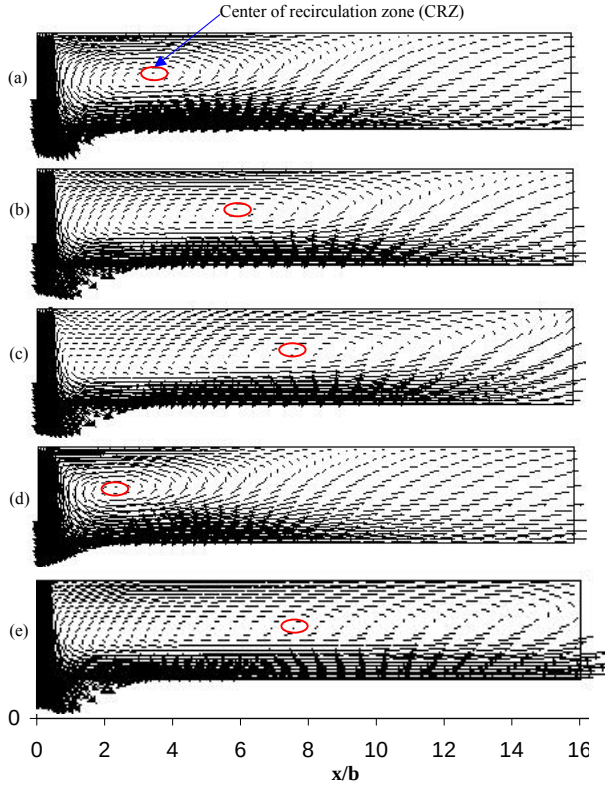

Figure 6 Velocity vector plot: (a) Standard k-ε, (b) RNG, (c) RSM, (d) k-ω, (e) SST.

In the neighborhood of stagnation region the flow is anisotropic as can be seen by the anisotropic ratio ($\overline{v'v'}/\overline{u'u'}$) distribution shown in Fig. 7(a). The highest anisotropic value reaches 8.5 near the wall at the locations x/b = 1 and 2. The anisotropic region spread wider from the stagnation region to x/b=2 and achieves better isotropy at x/b > 5. In Fig. 7 (b) the distribution of turbulent shear stress $\overline{u'v'}$ shows that active turbulent motion reaches its highest value around x/b =10 and decays downstream. As k-ε model predicts experimental results well next to RSM, it would be interesting to compare the turbulent viscosity calculated by these two models to understand their differences. Figures 8 (a) and (b) show the distribution of turbulent viscosity predicted by k-ε and RSM models at x/b = 1 and 2 to be distinctly different-- k-ε model predicts high turbulent viscosity near wall region.

Effect of computational domain – Since all the turbulence models except RSM do not predict the far-field wall temperature well beyond x/b =8, it was suspected that the scattered prediction data might be due to the selection of the computational domain (Fig. 1). The exit of the current computational domain (the basic domain) has been placed at the end of the confined channel, whereas in the actual test setup the fluid enters into a settling plenum from the confined channel before it is finally exhausted through a circular tube. Although the design of the settling plenum was meant to reduce the disturbances outside the test section from affecting the flow inside the channel, it

became necessary to include the settling plenum in the computational domain (the extended domain) to examine the effect of the extended computational domain on the far-field temperature data.

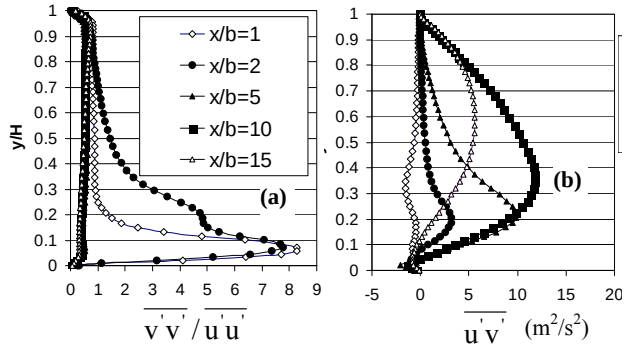

Figure 7 Distribution of (a) anisotropy and (b) Reynolds shear stress predicted by RSM model on the slot impingement jet.

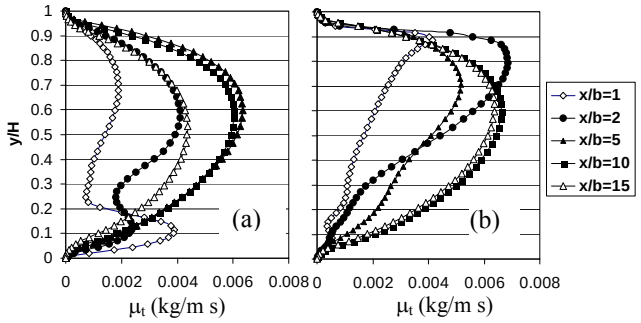

Figure 8 Distribution of turbulent viscosity calculated by (a) k-ε and (b) RSM turbulence models.

The result in Fig. 9 shows that using the extended domain reduces the far-field wall temperature values and does allow a better prediction of the wall temperature within 3°C at x/b=10. On the other hand the deviation between measured and computed values increases slightly at x/b = 7.5 when comparing the result of the basic model. Overall speaking, the extended domain predicts the temperature distribution trend better than the basic domain, especially in the far-field location. It is worth a note that the measured heat transfer data had 5 ~ 7 percentage uncertainty [4] that would cause the uneven deviation between measured and predicted data. As the present study focuses on cooling enhancement due to mist, which occurs mainly near the stagnation region, this bias error is self-compensated; therefore the basic computational domain model has been used for all cases and significant computation time has been saved.

Effect of various forces on the Discrete Phase Model (DPM) – After choosing RSM as the best-suited turbulence model for steam and steam/mist flows, computation was carried out to further tune the discrete phase model. As explained previously, the prediction of trajectory of a discrete phase particle is achieved by integrating the force balance on the particle. The dominant main forces are drag and gravitational.

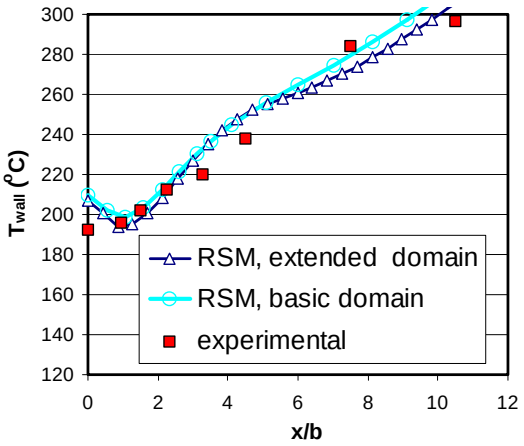

Figure 9 Effect of computational domain on slot impinging jet cooling (steam only).

In addition to the main forces, secondary forces like thermophoretic, Brownian and Saffman are included in the computation, and the effect of each additional force is investigated individually. Saffman force [28] concerns a sphere moving in a shear field. It is perpendicular to the direction of flow, originating from the inertia effects in the viscous flow around the particle. It can be given as:

$$F_{saff} = 1.615\rho\nu^{0.5}(u_g - u_p)(du/dn)^{0.5} \qquad (22)$$

where du/dn is the gradient of the tangential velocity. It is valid only when $Re_p << 1$.

The thermophoretic force arises from asymmetrical interactions between a particle and the surrounding fluid molecules due to temperature gradient. This force tends to repel particles or droplets from a high temperature region to a low temperature region. The following equation can be used to model this force:

$$F_n = -K\frac{1}{m_p T}\frac{\partial T}{\partial n} \qquad (23)$$

More details can be found in Talbot et al. [29]

Brownian force considers the random motion of a small particle suspended in a fluid, which results from the instantaneous impact of fluid molecules. It can be modeled as a Gaussian white noise process with spectral intensity given by [30].

Figure 10 shows the comparison of the experimental and computed target wall temperature distributions under influences of various forces by injecting 2% (wt.) mist into the steam flow. The wall temperature is approximately 20°C over- predicted near the stagnation point and under predicted 10-20°C at x/b > 2, if only the main drag and gravitational forces are considered. The effect of secondary forces on the wall temperature is negligible except at the stagnation region. The inclusion of Saffman force increases the accuracy of prediction noticeably in the stagnation region.

Effect of time scale used in the stochastic particle tracking – The prediction of stochastic particle dispersion makes use of the concept of the integral time scale, which describes the time spent in turbulent motion along the particle path [34]. The approximate time scale constant (TC) for the RSM model can be calculated from the empirical relation TC = 0.3 k/ε, where k is the turbulent kinetic energy and ε is dissipation rate. Based on this equation, the time constant for the studied cases are approximately 0.0005s. The value was arrived at taking maximum values of k and ε in the computational domain. Hence, the TC value varies thought out the domain (Fig. 12c). Different time constants including TC = 0.15, 0.005 and 0.0001s are provided to investigate the effect of time constant on the heat transfer result. The effect of different time scales on stochastic particle tracking is shown in Fig. 11, together with a case without employing a stochastic tracking scheme. The results show that the value TC =0.0005s gives a better match with the experimental results than all other options. The case without stochastic tracking predicts better than those cases with stochastic tracking but using an improper selection of TC values. The distribution of k, ε and TC for the steam only case is shown in Fig. 12. The maximum values of k and ε appear just near the lip of the jet inlet. Strong k can be also seen between x/b of 8 and 10.

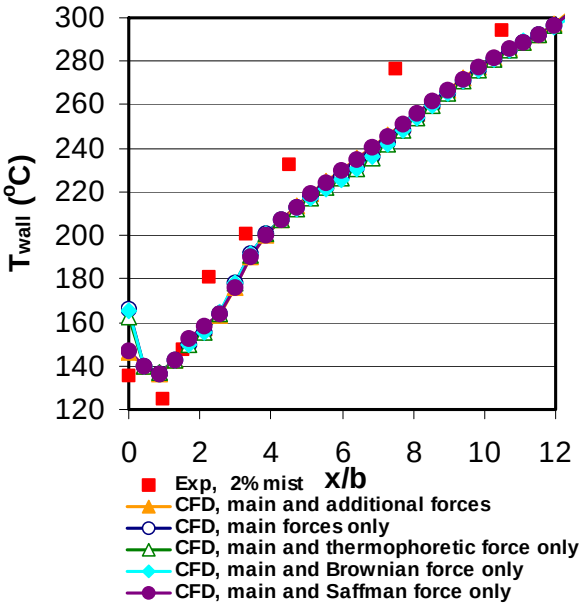

Figure 10 Effect of main and secondary forces of droplet model on slot impingement jet cooling (2% mist). Main forces include drag and gravitational forces.

Effect of mist/steam mass concentration ratio – After the above calibration, the tuned CFD model is used to predict mist cooling enhancement in impingement steam jets. Figure 13a shows the comparison between experimental and computational results of wall temperature distribution for the slot impingement jet for three cases: steam only, 1%, and 2% mist. The results show that the CFD model with the steam-only case predicts the wall temperature within 5% of the experimental data. In the cases of 1% and 2% mist, the CFD predictions are within 10% of the experimental data.

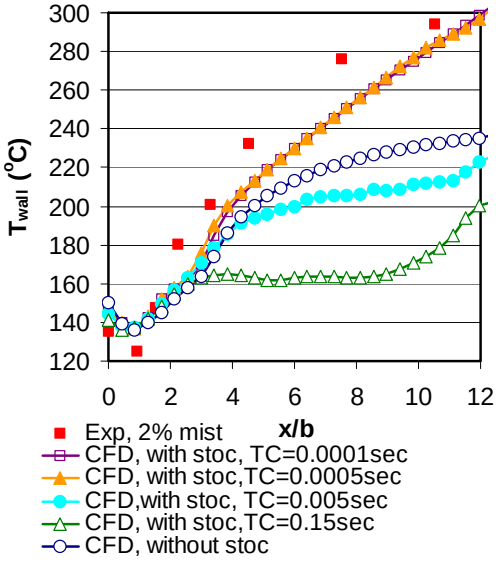

Figure 11 Effect of stochastic tracking time scale constant (TC) on the slot jet model.

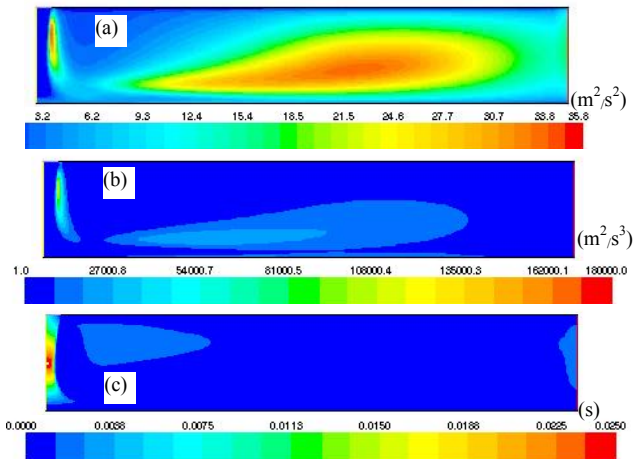

Figure 12 Distribution of (a) turbulent kinetic energy k (b) turbulent dissipation rate ε (c) TC (0.3 k/ε).

Distributions of heat transfer coefficient for the three cases are plotted in Fig. 13b. Here, the heat transfer coefficient is calculated as:

$$h(x) = q''/(T_w(x)-T_j) \qquad (24)$$

The steam saturation temperature at 105°C is taken as the jet temperature, and the constant wall heat flux q" is at 20,900 W/m^2. In the steam-only case, the result shows that the CFD model predicts the h-value very well in the entire surface, except at the stagnation line where the CFD model under predicts the h-value by about 10%. In the 1% mist case, the CFD model predicts the h-value well for region

x/b > 3 but over predicts the h-value by approximately 15% in the region of x/b < 2 and under predicts the stagnation line h-value. In the 2% mist case, the CFD model also predicts h-value well for x/b > 2 but under predicts the h-vale near the stagnation line for x/b < 2.

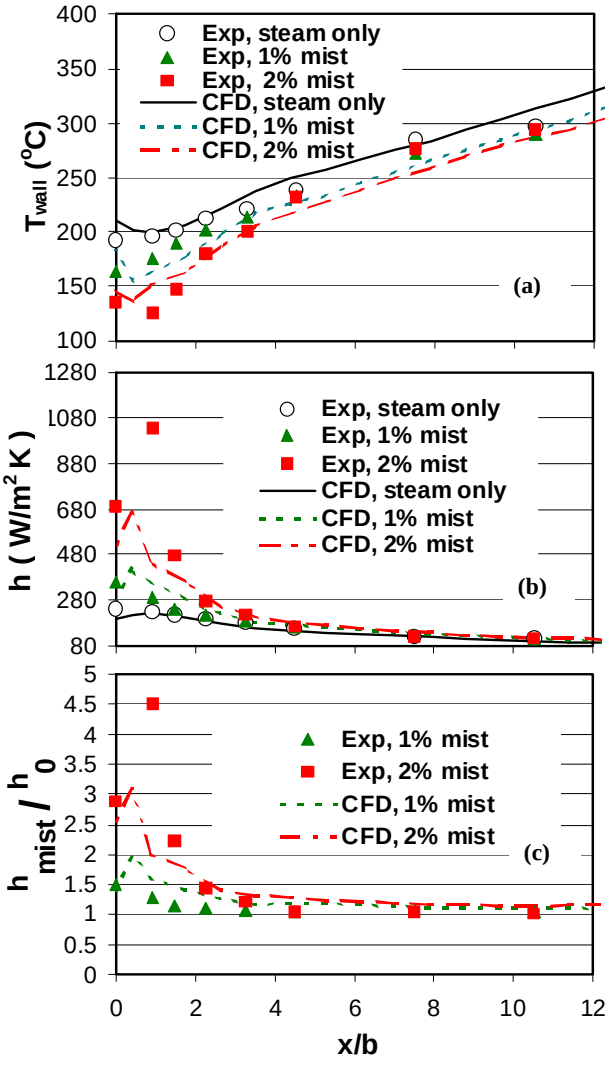

Figure 13 Heat transfer prediction of the slot impingement jet: (a) wall temperature, (b) heat transfer coefficient, and (c) cooling enhancement.

The enhancement ratio (h_{mist}/h_o) in Fig. 13c largely reflects the deviation trends of h-values. Overall, the CFD model can predict mist cooling wall temperature within ±10% and the h-value within ±20% from the experimental data. The above discussion bypassed one extremely high h-value (1000 W/m^2-K) in the experimental data at x/b = 1 of the 2% mist case. It needs to be noted that the prediction of heat transfer coefficient (h) and cooling enhancement ratio (h_{mist}/h_o) is not as accurate as the wall temperature because the wall temperature was directly measured, whereas the h-values and h_o/h_{mist} are derived by calculations. The h-value becomes very sensitive to any minor variation of wall temperature when cooling is effective, and the wall temperature approaches the saturation temperature (i.e., when T_w-T_j approaches zero, the heat transfer coefficient approaches infinity). This is what happens to the data at x/b=1. One option to avoid infinite large heat transfer coefficient is to replace the saturation temperature with the adiabatic wall temperature.

To obtain an idea of the water droplet evaporation rate, the surviving droplet mass concentration distributions across the channel height are plotted in Fig. 14 at various x/b locations. Fig. 14a shows the droplet mass concentration is confined near the wall within a layer of y/H = 0.18. The near-wall droplets evaporate and are consumed rapidly from x/b = 1 to 5. Beyond x/b = 5, the near-wall droplets deplete to almost zero within the region y/H <0.025. At the end of the test channel, plenty of droplets survive, as can be seen from the concentration distribution at x/b=10. A similar trend is observed for the 2% mist case shown in Fig. 14b.

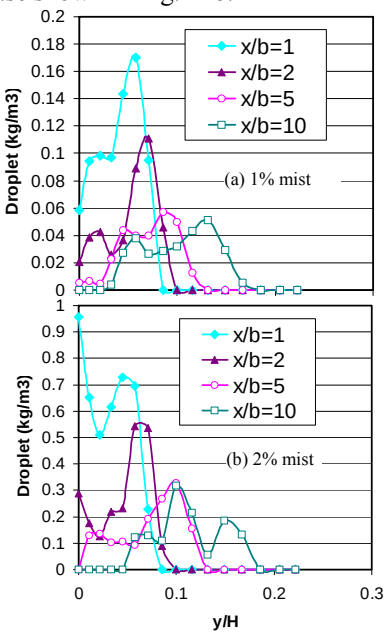

Figure 14 Droplet concentration distributions across the channel height at various x-locations of slot jet cases: (a) 1% and (b) 2% mist.

Results of Three-Row Impinging Jets

Effect of wall functions and y^+ values – From the predicted values of slot jet cases, it was shown that the near-wall Reynolds stresses calculation is very critical in computing wall temperature distribution. As these Reynolds stresses are calculated from the mean velocity shear, which is determined from the wall functions, choosing appropriate wall function is important. To make sure the calibrated CFD model is robust in 3-D flow predictions, the effect of wall functions in predicting target wall temperature is examined for three rows of impinging jets with steam-only case. Two types of wall functions, including standard wall and enhanced wall functions, are considered with the RSM turbulence model. Using a wall function during computation is meant to take advantage of the universal

law-of-the-wall behavior in the turbulent boundary layer to save computational time by not resolving the velocity profile in the near-wall region for $y^+ < 100$. In the 3-D impinging jet simulation, initially standard wall function with $y^+ \sim 20$ was used, as this value gave satisfactory results in 2D slot jet simulation. But in the 3-D application, there is an over prediction hump seen at x/b = 2 in Fig. 15. Then, the y^+ was further reduced to ~1 to see the effect of y^+ values. The results show that the hump is removed, the overall prediction matches the experimental data within 8%, and the temperature at the stagnation point is correctly predicted. The 8% wall temperature prediction band in a complex three-row impinging jets flow field is a much more significant achievement than 5% prediction band in a 2-D slot jet flow field.

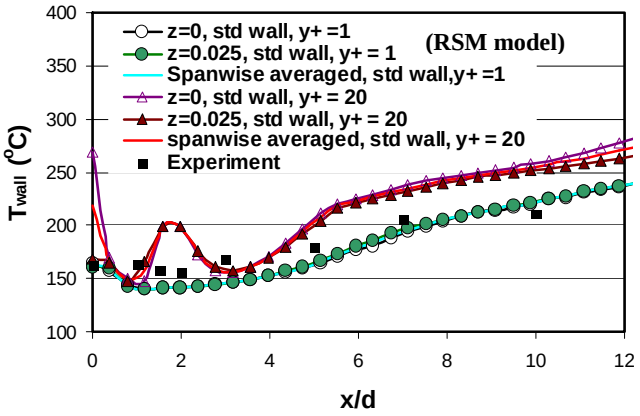

Figure 15 Effect of y^+ values of 1 and 20 with standard wall function on three-row impinging jets model (steam only).

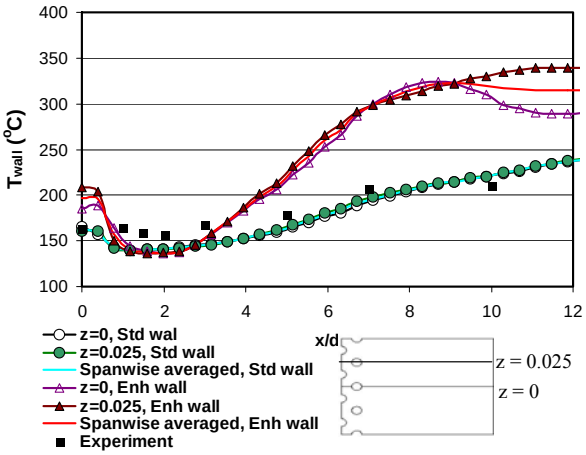

Figure 16 Effect of near-wall functions at $y^+ \sim 1$ on three-row impinging jets (steam only).

A further comparison between the standard wall function and the enhanced wall function with $y^+ \sim 1$ in Fig. 16 shows the standard wall function model outperforms the enhanced wall function model. The probable reason for the better performance of standard wall function than the enhanced wall function would be that it is designed for high Reynolds number flow and the wall function uses stress-strain relationship for the y^+ values less than 11.225 [34].

An additional computation has been performed on 3-D impinging jet case with SST model. But, the converged solution could not be obtained even the relaxation factors have been reduced down to 0.15 or when the converged results from RMS method was used as the initial conditions.

Prediction of mist cooling enhancement – After gaining confidence from the wall-function calibration, the fine-tuned CFD is then used to simulate the cooling enhancement with 1.5% mist injection into three rows of steam impinging jets. Fig. 17a shows that the CFD prediction of wall temperature with maximum deviation of 9% from experimental values for the steam-only case, while the prediction for the 1.5% mist case is very good with a deviation of only 2-3%. The data presented in Fig. 17 are taken from z=0 location i.e., centerline of the second row jet (see Fig. 18). Figure 17b shows CFD under predicts heat transfer coefficient (h) in steam-only case but fairs well with 1.5% mist case except at x/b=1.5, h-value is 20% under predicted. The CFD adequately predicts the off-axis maximum cooling at x/b = 2.

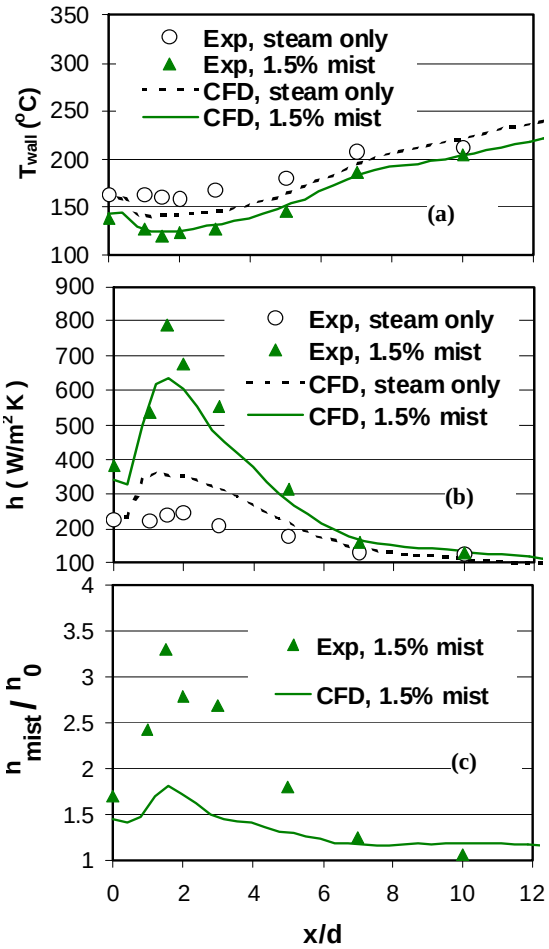

Figure 17 Heat transfer results of three-row jets: (a) wall temperature, (b) heat transfer coefficient and (c) ratio of heat transfer coefficient (enhancement) at centerline of the second jet hole (z=0.025).

Due to the over-predicted steam-only h-values and the under predicted mist h-values, the cooling enhancement (h_{mist}/h_o) prediction is significantly lower than the experimental data, as shown in Fig. 17c. Again, this is caused by the reason stated earlier that the h-value becomes very sensitive to any minor variation of wall temperature when cooling is effective and the wall temperature approaches the saturation temperature. The ratio of h_{mist}/h_o further amplifies this effect. For example, at x/b = 1.5 the experimental data are T_w = 120°C and h = 788 W/m^2-K, while the predicted wall temperature is at 124°C. This 4°C difference results in a h-value of 637 W/m^2-K (or 20% off).

The predicted contours of wall temperature and heat transfer coefficient shown in Fig. 18a and b illustrate the highly nonuniform surface temperature and heat transfer distribution with 1.5% mist. In the region of x/b = 4 to 7, a relatively uniform temperature distribution is seen due to spreading interaction between adjacent jets. Fig. 18a also shows the regions of high temperature at the exit from x/b = 12 to 16 due to fading cooling effect. The sidewalls produce a locally high temperature region near the wall at the exit. Due to this large nonuniform lateral distribution of temperature and heat transfer coefficient, using spanwisely averaged data to do comparisons would provide more stable and certain results. Unfortunately, the thermocouple data from the experiment can only provide two rows of data points.

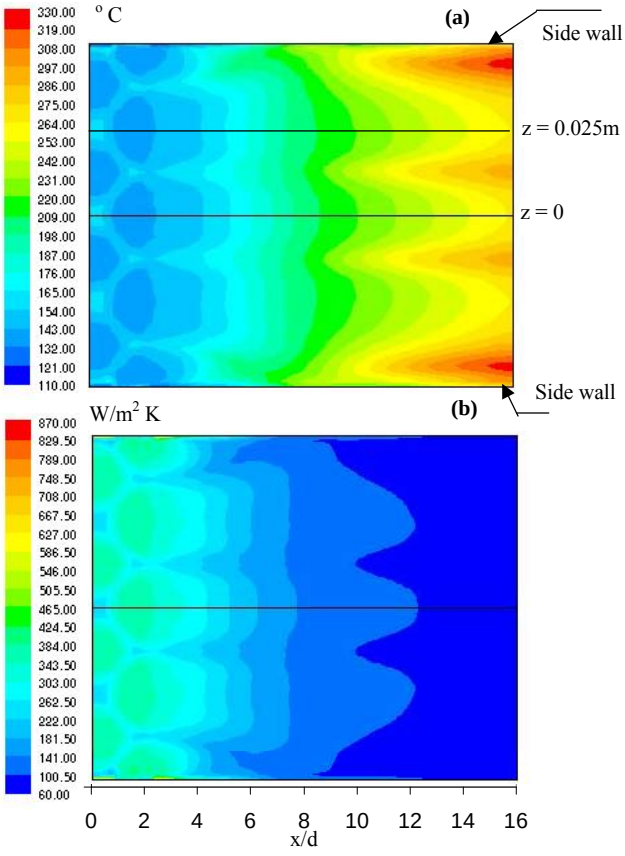

Figure 18 Contours of three-row jets with 1.5% mist: (a) temperature and (b) heat transfer coefficient.

CONCLUSIONS

A CFD model has been calibrated against the available experimental results of injecting fine-droplet mist into steam impinging jets of two arrangements a slot jet and three rows of jets. The following conclusions are drawn:

- The calibration process reveals that the RSM turbulence model with standard wall function gives better results on this application. The standard wall function works satisfactorily on 2-D flows with y^+ being set at 20 without needing to resolve the near-wall flow. However, in the 3-D flow, the calibration process requires resolution to the near-wall flow down to $y^+ \approx 1$. The selection of extended computational domain does affect the prediction of wall temperature at the far-field locations to approximately 2%, but not significantly.
- Drag force and droplet weight are the main forces affecting droplet dynamics. Among various secondary forces, Saffman force has been identified as an important factor that affects a more accurate prediction near the stagnation region. Other forces like thermophoretic and Brownian have a negligible effect on the predicted results.
-
- The stochastic tracking with time scale evaluated with 0.3k/ε provides better results.
- The calibrated CFD model can predict the wall temperature of the 2-D mist/steam slot impinging jet flow within 5% and the 3-D multiple rows of impinging jets within 8%.
- The h-value becomes very sensitive to any minor variation of wall temperature when cooling is effective, and the wall temperature approaches the saturation temperature. Therefore, comparisons between the experimental and CFD results are more certain by comparing wall temperatures rather than the h-values.
- This study's ultimate assessment -- drag, heat transfer, and evaporation models in the discrete phase are adequate, and the overall Eulerian (continuous phase) and Largrangian (discrete phase) of this calibrated model are ready to be used for predicting mist/steam cooling under real operating gas turbine conditions.

ACKNOWLEDGEMENTS

This study was supported by the Louisiana Governor's Energy Initiative via the Clean Power and Energy Research Consortium (CPERC) and administered by the Louisiana Board of Regents.

REFERENCES

[1] Guo, T., Wang, T., and Gaddis, J.L., 2000, "Mist/steam cooling in a heated horizontal tube: Part 1: Experimental system," ASME J. Turbomachinery, 122, pp.360-365.

[2] Guo, T., Wang, T., and Gaddis, J.L., 2000, "Mist/steam cooling in a heated horizontal tube: Part 2: Results and modeling," ASME J. Turbomachinery, 122, pp.366-374.
[3] Guo, T., Wang, T., and Gaddis, J.L., 2000, "Mist/steam cooling in a 180-degree tube," ASME J. Heat Transfer, 122, pp. 749-756.
[4] Li, X., Gaddis, T., and Wang, T., 2001, "Mist/steam heat transfer of confined slot jet impingement," ASME J. Turbomachinery, 123, pp.161-167.
[5] Li, X, Gaddis, J.L., and Wang, T., 2003, "Mist/steam heat transfer with jet impingement onto a concave surface," ASME J. Heat Transfer, 125, pp. 438-446.
[6] X. Li, Gaddis, T., and Wang, T., 2003, "Mist/steam cooling by a row of impinging jets," Int. J. Heat and Mass Transfer, 46, pp. 2279-2290.
[7] Wang, T., Gaddis, J. L., and Li, X., 2005, "Mist/steam heat transfer of multiple rows of impinging jets," Int. J. Heat and Mass Transfer, 48, pp. 5179-5191.
[8] Li, X, Gaddis, J.L., and Wang, T., 2001, "Modeling of heat transfer in a mist/steam impinging jet" ASME J. Heat Transfer, 123, pp. 1086-1092.
[9] Chou, Y.J., and Hung, Y.H., 1994, "Impingement cooling of an isothermally heated surface with a confined slot jet," ASME, J. Heat Transfer, 116, pp. 479-482.
[10] Chou, Y.J., and Hung, Y.H., 1994, "Fluid flow and heat transfer of an extended slot jet impingement," J. Thermophys. Heat transfer, 116, pp. 538–545.
[11] Laschefski, H., Cziesla., Biswas, G., and Mitra, N.K., 1996, "Numerical heat transfer by rows of rectangular impinging jets," Numer. Heat Transfer, 30, pp.87-101.
[12] Cziesla, T., Tandogan, E., Mitra, N.K., 1997, "Large eddy simulation of heat transfer from impinging slot jets," Numer. Heat Transfer, 32, pp.1-17.
[13] Yang, Y.T., and Shyu, C.H., 1998, "Numerical study of multiple impinging slot jets with an inclined confinement surface," Nume. Heat Transfer, 33, pp.23-37.
[14] Tzeng, P.Y., Soong, C.Y., and Hsieh, C.D., 1999, "Numerical investigation of heat transfer under confined impinging turbulent slot jets," Numer. Heat Transfer, 35, pp.903-924.
[15] Goodro, M., Park, J., Ligrani, P., Fox, M., and Moon, H.K, 2007, "Effect of hole spacing on jet array impingement heat transfer," ASME Turbo Expo 2007 (GT2007-28292), Montreal, Canada, May 2007.
[16] Shimizu, A., Echigo, R., and Hasegawa, S., 1979, "Impinging jet heat transfer with gas-solid suspension medium", Heat Transfer Conference., San Diego, California, pp.155-160.
[17] Yoshida, H., Suenaga, K., and Echigo, R., 1990, "Turbulence structure and heat transfer of a two-dimensional impinging jet with gas-solid suspensions," Int. J. Heat Mass Transfer, 33, no. 5, pp.859-867.
[18] Li, X., and Wang, T., 2005, "Simulation of Film cooling enhancement with mist injection," ASME Journal of Heat transfer, 128, pp.509-519.
[19] Li, X. and Wang, T., 2005, "Effects of various modelling on mist film cooling," Proc. ASME Int. Mechanical Engineering Congress and Exhibition (IMECE 2005-81780), Orlando, Florida, November 2005.
[20] Li, X., and Wang, T., 2007, "Two-Phase Flow Simulation of Mist Film Cooling on Turbine Blades with Conjugate Internal Cooling" to appear in ASME Journal of Heat Transfer.
[21] Terekhov, V.I., and Pakhomov, M.A., 2006, "Numerical Study of the Near-Wall Droplet Jet in a Tube with Heat Flux on the Surface", J. Apll. Mech. Tech. Physics, 47, pp. 1-11.
[22] Li, X., and Wang, T., 2007, "Computational analysis of surface curvature effect on mist film cooling performance," Proc. of TurboExpo 2007, ASME paper GT2007-27434, Montreal, Canada, May, 2007.
[23] Launder, B.E., and Spalding, D.B., 1972, Lectures in Mathematical Models of Turbulence, Academic Press, London, England.
[24] Wolfstein, M., 1969, "The velocity and temperature distribution of one-dimensional flow with turbulence augmentation and pressure gradient, "Int. J. Heat Mass Transfer, 12, pp. 301-318.
[25] Choudhury, D., 1993, Introduction to the Renormalization Group Method and turbulence modeling, Technical Memorandum, TM-107, Fluent Inc.
[26] Wilcox, D.C., 1998, Turbulence modeling for CFD, DCW Industries, Inc., La Canada, California.
[27] Menter, F, 1993, "Zonal two equation model for aerodynamic flows," AIAA paper 93-2906.
[28] Saffman, P.G., 1965, "The lift on a small sphere in a slow shear flow," J. Fluid Mech., 22, pp. 385-400.
[29] Talbot, L., Cheng, R. K., Schefer, R. W., and Willis, D. R., 1980, "Thermophoresis of particles in a heated boundary layer,"J. Fluid Mech., 101, pp.737-758.
[30] Li, A., and Ahmadi, G., 1992, "Dispersion and deposition of spherical particles from point sources in a turbulent channel flow,", Aerosol Science and Technology, 16, pp. 209-226.
[31] Ranz, W. E., and Marshall, W. R. Jr., 1952, "Evaporation from drops, Part I, "Chem. Eng. Prof., 48, pp. 141-146.
[32] Ranz, W. E., and Marshall, W. R. Jr., 1952, "Evaporation from drops, Part II, "Chem. Eng. Prof., 48, pp. 173-180.
[33] Kuo, K. Y., 1986, Principles of combustion, John Willey and Sons, New York.
[34] Fluent Manual, Version 6.2.16,2005, Fluent Inc.